Progress in Natural Science: Materials International 36 (2026) 187–194

HOSTED BY

Contents lists available at ScienceDirect

Progress in Natural Science: Materials International

journal homepage: www.elsevier.com/locate/pnsmi

Enhanced room-temperature hydrogen response of TiO_2 nanotube Schottky device through carrier transport modulation

Xiaochuan Long[a,b,c,d], Xiao Wen[b,c,d], Xiao Zhang[b,c,d], Zheng Lu[a], Feng Wei[b,e], Xiaopeng Liu[b,c,d,*]

[a] School of Materials Science and Engineering, Northeastern University, Shenyang, 110819, China
[b] State Key Laboratory of Advanced Materials for Intelligent Sensing, China GRINM Group Co. Ltd., Beijing, 100088, China
[c] GRIMAT Engineering Institute Co. Ltd., Beijing, 101407, China
[d] General Research Institute for Nonferrous Metals, Beijing, 100088, China
[e] GRINM (Guangdong) Institute for Advanced Materials and Technology, Foshan, 528000, China

ARTICLE INFO

Keywords:
Hydrogen sensor
TiO_2 nanotubes
Titanium film
Anodic oxidation

ABSTRACT

Fabricating TiO_2 nanotube hydrogen sensors via anodic oxidation of sputtered Ti films on Si wafers enhances stability and facilitates integration/miniaturization. However, these sensors exhibit lower room-temperature responses compared to counterparts derived from anodized Ti thin sheets. In this work, Pt/TiO_2/Ti sensors incorporating an unoxidized Ti film at the nanotube base and Pt/TiO_2 sensors with completely oxidized Ti foil were fabricated on SiO_2/Si substrates through magnetron sputtering and anodic oxidation. The Pt/TiO_2/Ti sensor exhibited a response of 5.3×10^6 toward 200 ppm H_2 at room temperature – four orders of magnitude higher than the Pt/TiO_2 counterpart. Through SEM, Hall measurements, and I-V analysis, this enhancement is attributed to significantly reduced charge transfer resistance between Pt interdigitated electrodes (IDEs) due to the conductive Ti film in Pt/TiO_2/Ti devices. The modulating effect of the Ti film on carrier transport pathways becomes more pronounced at lower operating temperatures. This study provides a straightforward yet effective approach for developing high-responsivity TiO_2 nanotube hydrogen sensors on silicon wafers.

1. Introduction

Hydrogen sensors are of pivotal importance in industrial facilities, transportation networks and renewable energy systems. Metal oxide semiconductors (MOS), including ZnO, SnO_2, TiO_2 and Co_3O_4, have attracted considerable research interest for hydrogen owing to their exceptional gas reactivity sensitivity [1–4]. The gas-sensing performance of MOS can be effectively enhanced by increasing its specific surface area and optimizing the device structure [5–7]. TiO_2 nanotubes are of particular note due to their large surface areas, suitable bandgap, and highly ordered structure. These properties position them as promising candidates for high-performance hydrogen sensing [8,9].

TiO_2 nanotube-based hydrogen sensors fabricated via anodic oxidation of Ti thin sheets demonstrated exceptional room-temperature detection capabilities, exhibiting a response magnitude of $10^{8.7}$–1000 ppm H_2 [10,11]. However, the inherent mechanical flexibility of the titanium sheets induces bending deformation, resulting in electrical short-circuiting between the platinum electrodes and the underlying titanium substrate. These configurations face significant challenges in terms of miniaturization and system integration, severely limiting their practical applicability [12–15]. Consequently, fabricating TiO_2 nanotube-based sensors via anodic oxidation of Ti foil sputtered onto rigid substrates may present a viable solution. However, studies indicate that replacing titanium sheets with sputtered Ti foils on rigid substrates for anodic oxidation results in significantly degraded gas-sensing performance in the resulting TiO_2 sensors. For example, fabrication strategies employing titanium-coated glass or ceramic substrates exhibit compromised sensing performance, exhibiting a 10,000-fold reduction in response magnitude compared to nanotube sensors derived from anodized titanium sheet [16,17]. Moreover, silicon-based substrates have emerged as a compelling alternative platform, offering superior compatibility with microelectromechanical systems fabrication processes [18]. The response magnitude of TiO_2 nanotube sensors directly fabricated on silicon substrates was found to be 10^3 at 180°C for 1000 ppm H_2 [19,20]. In contrast, partially anodized titanium patterns with platinum modification on silicon substrates

* Corresponding author. State Key Laboratory of Advanced Materials for Intelligent Sensing, China GRINM Group Co. Ltd., Beijing, 100088, China.
E-mail address: xpgliu@grinm.com (X. Liu).

https://doi.org/10.1016/j.pnsc.2026.01.006
Received 14 November 2025; Received in revised form 29 December 2025; Accepted 19 January 2026
Available online 9 February 2026

exhibited enhanced response magnitudes of 10^7 at 300°C for 1% H_2 [18, 21]. Table 1 summarizes the response characteristics of TiO_2 nanotube sensors fabricated on various substrates. In comparison to the TiO_2 nanotube sensors prepared on Ti substrates, as reported in Ref. [10], those built on insulating substrates show a lower response value and function at higher temperatures. This performance discrepancy suggests that maintaining a conductive titanium interlayer beneath the TiO_2 nanotube arrays, forming TiO_2/Ti heterostructures, could substantially enhance hydrogen sensing capabilities compared with pure TiO_2 nanotube configurations directly grown on silicon substrates. To investigate this hypothesis, two distinct hydrogen sensors—Pt/TiO_2/Ti and Pt/TiO_2 architectures—were fabricated on silicon thermal oxide wafer substrates through a sequential integration of magnetron sputtering and anodic oxidation. This study systematically examines the hydrogen sensing mechanisms, with particular emphasis on elucidating the critical role of titanium interlayers in enhancing gas sensor performance.

2. Experiment

A 1.8-μm-thick foil of titanium was deposited on thermally oxidized silicon 4-inch wafers (SiO_2/Si) substrates via direct current (DC) magnetron sputtering, using a titanium target (60 mm diameter × 5 mm thickness, 99.995% purity, ZhongNuo Advanced Material (Beijing) Technology Co., Ltd, Beijing, China). The deposition process was conducted under the following optimized conditions: a fixed target-to-substrate distance of 20 mm, a substrate temperature maintained at 200°C, a base pressure of 2.0×10^{-4} Pa, an argon working pressure of 0.3 Pa, sputtering time of 1 h, and a power density of 3.18 W/cm^2. The as-deposited Ti/SiO_2/Si samples were then cut into 10 mm × 30 mm specimens for subsequent anodic oxidation, as illustrated in Fig. 1a. This oxidation was performed in an ethylene glycol electrolyte containing 0.2 M ammonium fluoride (NH_4F) and 3 vol.% ultrapure water [22]. The Ti foil on the Ti/SiO_2/Si was oxidized at a constant DC voltage of 45 V

Table 1
Response characteristics of TiO_2 nanotubes hydrogen gas sensors fabricated on various substrates.

Material	Electrode	Substrate	Testing temperature	Concentration (ppm)	Response	Ref.
TiO_2	Pt	Ti sheet	RT	1000 ppm	$10^{8.7}$	[10]
TiO_2	Pt	Ti sheet	RT	200 ppm	822.9	[11]
TiO_2	Au	Ti sheet	RT	1000 ppm	8.5	[12]
TiO_2	Pd	Ti sheet	RT	10000 ppm	1200	[13]
TiO_2	Pt	Ti sheet	150°C	1000 ppm	28	[14]
RGO/TiO_2	Pt	Al_2O_3	200°C	480 ppm	37.6	[16]
TiO_2	Pt	Glass	RT	1000 ppm	10^4	[17]
TiO_2	Ti	SiN/Si	300°C	1000 ppm	50	[18]
Pd/TiO_2	Al/Au	SiO_2/Si	180°C	1000 ppm	1000	[19]
Pt/TiO_2	Ti	SiN/Si	300°C	100 ppm	10^4–10^5	[21]
TiO_2	Pt	SiO_2/Si	RT	200 ppm	517	This work
TiO_2/Ti	Pt	SiO_2/Si	RT	200 ppm	5.2×10^6	This work

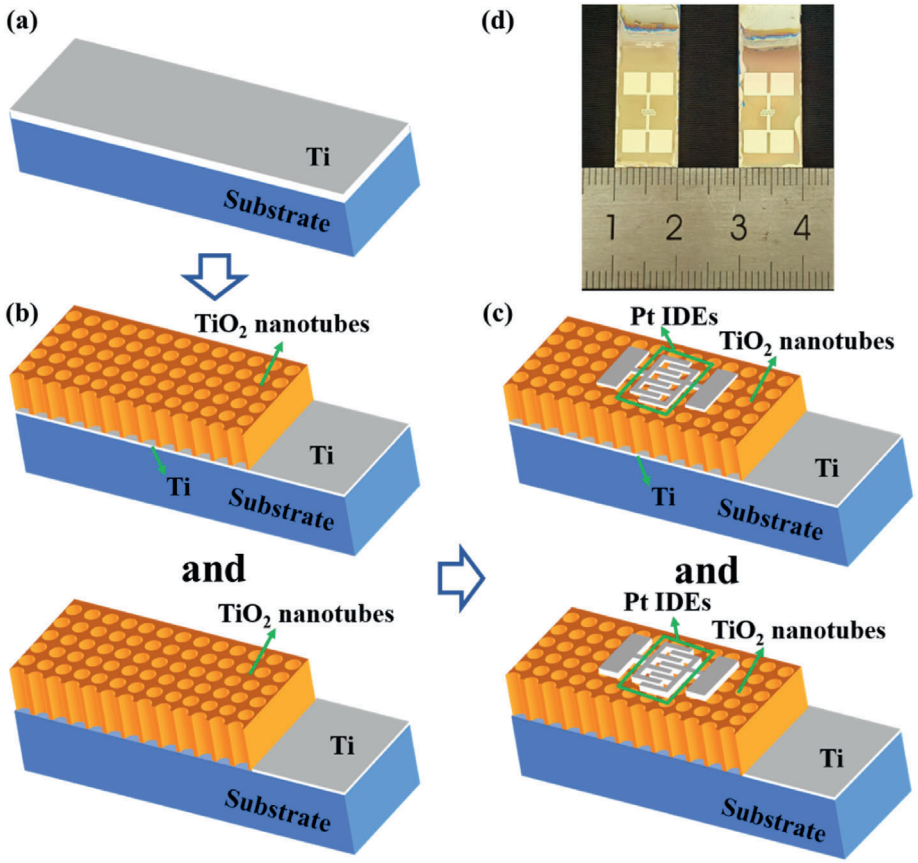

Fig. 1. Schematic illustration of the gas sensor fabrication process: (a) Deposition of Ti foil on SiO_2/Si substrate; (b) Anodic oxidation of Ti foil; (c) Deposition of Pt IDEs on TiO_2 nanotubes and heat treatment. (d) Photograph of the Pt/TiO_2/Ti (left) and Pt/TiO_2 sensors (right).

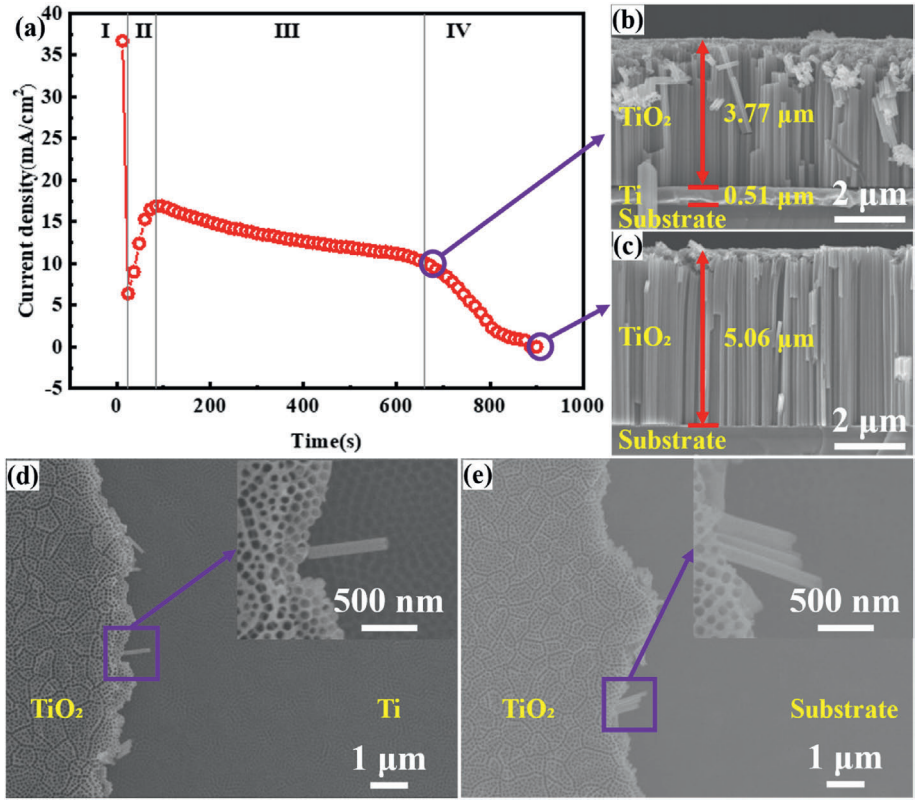

Fig. 2. (a) Current density–time profile recorded during the anodic oxidation process. Cross-sectional SEM images of samples anodized at a current density cutoff of (b) 9 mA/cm^2 and (c) 0 mA/cm^2. Top-view images of samples after partial TiO_2 nanotube arrays removal, obtained at current densities of (d) 9 mA/cm^2 and (e) 0 mA/cm^2.

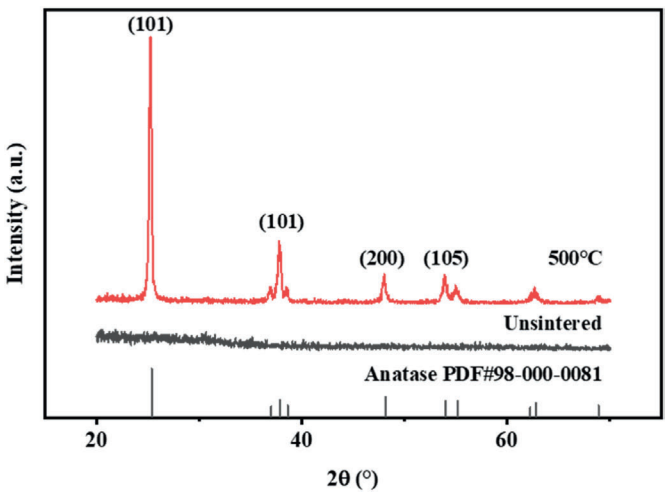

Fig. 3. GIXRD patterns of the TiO_2 nanotubes before and after sintered at 500°C.

and 20°C for a specific duration. During the anodization process, the current was monitored in real time. The anodization process was terminated upon reaching current densities of 9 mA/cm^2 and 0 mA/cm^2, respectively. The samples shown were washed with ultrapure water for 30 s following anodization and then dried under a nitrogen gas flow (0.1 Mpa), yielding both TiO_2/Ti and TiO_2 samples as illustrated in Fig. 1b. The next step involved the patterning of platinum interdigital electrodes (Pt IDEs) (150 μm width, 500 μm length, and inter-electrode spacing of 100 μm) on the TiO_2 nanotubes of samples (Fig. 1c). This patterning process was facilitated through the use of a shadow mask with magnetron sputtering. Finally, the samples underwent annealing at 500°C for 2 h in air with heating and cooling rates of 2°C/min [12]. Fig. 1d presents the macro-morphology of the Pt/TiO_2/Ti and Pt/TiO_2 sensors.

Table 2
Hall effect measurements of TiO_2.

Sample	ρ(Ω·cm)	Carrier mobility (cm^2/(V·S))	Carrier concentrations (cm^{-3})	Hall coefficient (cm^3/C)
TiO_2	1.44×10^4	1.27	3.41×10^{14}	-1.83×10^4

The morphologies and microstructures of the sensors were observed using scanning electron microscopy (SEM; JSM-7610F PLUS) at an acceleration voltage of 5 kV. Carrier mobility and concentration were determined by Hall measurement (Accent HL5500) at 0.5 T magnetic field with applied currents from −200 mA to 200 mA. The current-voltage (I-V) characteristics of the sensors under ambient conditions and hydrogen exposure were measured using a semiconductor parameter analyzer (Keithley 4200-SCS). The gas sensor was hermetically sealed in an aluminum chamber (80 mm diameter × 30 mm depth), with its Pt IDEs utilized for real-time signal acquisition. A gas flow rate of 500 mL/min was employed. The sensor current in both target gas and dry air environments was recorded using a picoammeter (Keithley 6487) at 5 V bias. Measurements were performed over a working temperature range of 27–300°C, with a 10-min dry air stabilization period prior to testing at each temperature. Sensing tests were conducted in synthetic dry air and target gas mixtures. All gases used in the experiments were prepared and supplied at specified concentrations by Air Products and Chemicals, Inc. Beijing Branch. The sensor response is defined as I_{Air}/I_{gas} under reductive atmospheres, whereas under oxidative atmospheres it is defined as I_{gas}/I_{Air}, where I_{Air} and I_{gas} represent the current in air and the target gas, respectively. The response time and recovery time are defined as the durations required for the sensor current to reach 90%

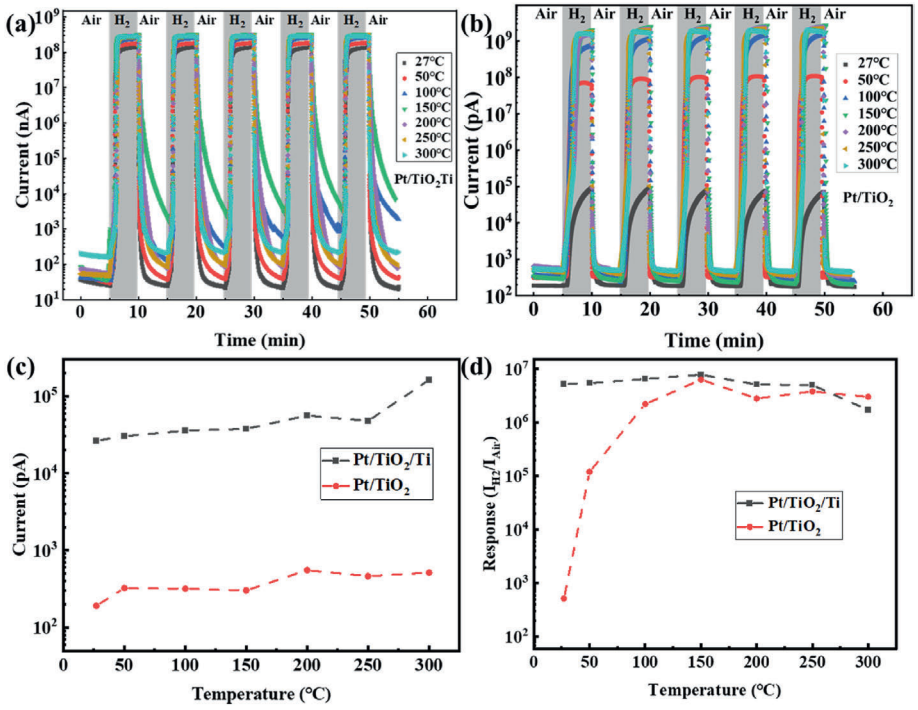

Fig. 4. (a) Temperature-dependent response-recovery curves of Pt/TiO_2/Ti sensor to 200 ppm hydrogen; (b) Corresponding response-recovery curves of Pt/TiO_2 sensor. (c) Baseline currents of sensors at various operating temperatures (RT to 300°C). (d) Hydrogen response magnitudes of sensors at different temperatures.

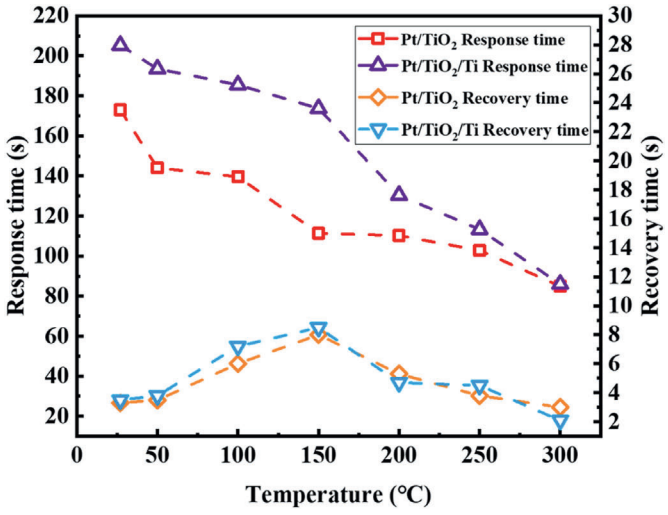

Fig. 5. Response and recovery times of Pt/TiO_2/Ti and Pt/TiO_2 sensors.

and 10% of the total change during H_2 exposure and air recovery, respectively.

3. Results and discussion

Fig. 2a presents the current density-time curve during the anodic oxidation of Ti foils sputtered on SiO_2/Si substrates, revealing four characteristic stages [23,24]. By employing 9 mA/cm^2 as the cutoff current density, a TiO_2/Ti composite structure was fabricated, comprising a residual Ti underlayer (0.51 μm thick) and a surface-anchored TiO_2 nanotube arrays (3.77 μm in thickness), as illustrated in Fig. 2b. The volume expansion phenomenon induced by anodic oxidation exhibits consistency with prior reports [25]. In comparison, when the current density stabilized at 0 mA/cm^2, the nanotube arrays thickness was 5.06 μm (Fig. 2c). Morphological characterization was conducted on the samples prepared at 9 mA/cm^2 after removing part of nanotubes (Fig. 2d). The magnified region in Fig. 2d reveals corrosion pits formed on the surface of the unoxidized Ti foil at the nanotube base, consistent with previous studies [26–28]. The sample exhibits a smooth SiO_2/Si substrate after part of nanotubes removal, indicating that the Ti foil was completely oxidized (Fig. 2e). The nanotubes in both samples exhibit comparable wall thicknesses of ~20 nm, as quantitatively confirmed by SEM analysis. The Pt/TiO_2/Ti and Pt/TiO_2 sensors were fabricated using a TiO_2/Ti nanocomposite layer and pure TiO_2 nanotube arrays, respectively.

Identical sintering processes were employed for both Pt/TiO_2/Ti and Pt/TiO_2 sensors, ensuring consistent material properties of TiO_2 and identical Pt-TiO_2 interfaces. Fig. 3 illustrates that the TiO_2 nanotubes are initially in an amorphous phase following anodization, which subsequently transforms into the anatase phase upon sintered at 500°C. Table 2 presents Hall effect measurement results for TiO_2. The negative Hall coefficient confirms TiO_2 as an n-type semiconductor [29]. Carrier concentration in TiO_2 nanotubes is over 1000 times lower than in TiO_2 thin foils reported in Refs. [30,31], arising from the difference in the concentration of negatively charged adsorbed oxygen species on the TiO_2 surface. The process of oxygen adsorption on the TiO_2 surface facilitates electron transfer from the TiO_2 matrix to adsorbed oxygen species, generating electron depletion layers within the TiO_2 [32]. The higher specific surface area of TiO_2 nanotubes relative to thin foils promotes greater surface-adsorbed oxygen concentration, correspondingly reducing carrier concentration.

Fig. 4a and b displays the hydrogen-sensing response-recovery curves of the Pt/TiO_2/Ti and Pt/TiO_2 sensors toward 200 ppm H_2 across a temperature range from room temperature (27°C) to 300°C, respectively. Under identical testing conditions, the Pt/TiO_2/Ti sensor exhibited higher current than the Pt/TiO_2 sensor. Fig. 4c displays current values for both sensors in air at various temperatures. As shown in Fig. 4c, the baseline current of the Pt/TiO_2/Ti sensor was approximately 100-fold greater than that of the Pt/TiO_2 sensor. In Fig. 4d, response magnitudes of the sensors at different temperatures indicate identical optimal operating temperatures of 150°C for both devices. However, at

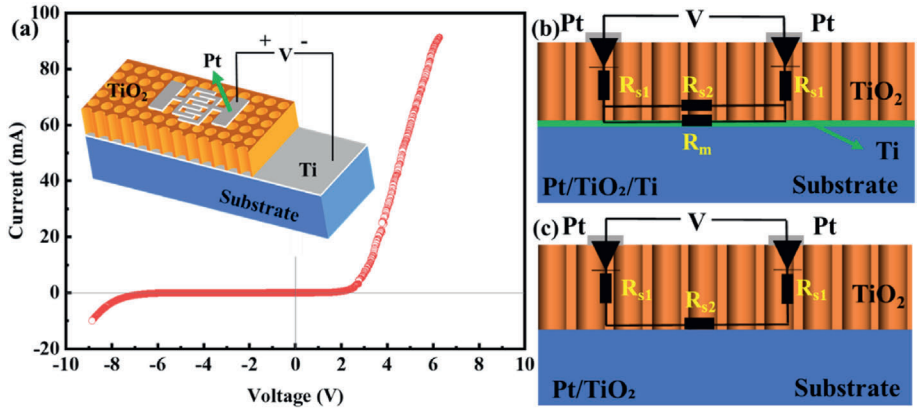

Fig. 6. (a) Current-Voltage (I–V) characteristics of Pt/TiO_2/Ti sensor in air at room temperature, with an inserted figure illustrating the curve acquisition circuit diagram. (b) Equivalent circuit model of the Pt/TiO_2/Ti sensor obtained from the date in (a). (c) Equivalent circuit model of the Pt/TiO_2 sensor.

room temperature, the Pt/TiO_2/Ti sensor demonstrated ~10,000 times higher response magnitude than the Pt/TiO_2 sensor, with this disparity diminishing as operating temperature increased. Fig. 5 presents the response and recovery times of Pt/TiO_2/Ti and Pt/TiO_2 sensors within the tested temperature range. Increasing the operating temperature accelerates the reaction between H_2 and surface-adsorbed oxygen, resulting in a decrease in the response time of the sensors with rising temperature. When the ambient gas is switched from the target gas to air, oxygen adsorbs on the TiO_2 surface, and electrons from TiO_2 transfer to the surface-adsorbed oxygen, leading to a decrease in the electrical conductivity of the sensor. At temperatures $\leq$150°C, the concentration of surface-adsorbed oxygen on the TiO_2 surface increases with temperature, which enhances the gas-sensing response. However, this also prolongs the time required to reach equilibrium during recovery in air, resulting in the longest recovery time at 150°C. When the temperature exceeds 150°C, the desorption rate of oxygen from the TiO_2 surface increases, reducing the surface-adsorbed oxygen concentration [33]. Consequently, the gas-sensing response decreases with further temperature increase, and the recovery time of the sensor shortens.

The fundamental distinction between the two sensors lies in the presence of an unoxidized Ti film at the base of the TiO_2 nanotubes in the Pt/TiO_2/Ti sensor, absent in the Pt/TiO_2 counterpart. The significant disparity in room-temperature gas-sensing performance between the two sensors likely arises from their structural differences. To investigate the role of the Ti interlayer, current-voltage (I-V) characteristics were measured on the Pt/TiO_2/Ti sensor with half of the Pt IDEs as the anode and the bottom Ti film as the cathode. A schematic diagram of the test circuit is shown in the inset of Fig. 6a. The sensor exhibited unidirectional conductivity: under forward bias, current increased significantly beyond the threshold voltage with linear behavior attributable to diode series resistance [31]. Conversely, under reverse bias, minimal current was observed until breakdown voltage, whereupon rapid current increase occurred. This rectifying behavior originates from work function differences among TiO_2 (4.4 eV), Pt (5.3 eV), and Ti (4.3 eV) [34–37]. Specifically, a Schottky barrier forms at the Pt–TiO_2 interface due to significant work function mismatch, while an Ohmic contact develops at the Ti–TiO_2 interface.

The equivalent circuit of the Pt/TiO_2/Ti sensor, as derived from the I-V characteristics in Fig. 6a, is presented in Fig. 6b [12,31]. The circuit model comprises four key components: (1) a Schottky diode representing the Pt/TiO_2 interface, (2) R_{s1} corresponding to the resistance of the TiO_2 layer sandwiched between the upper Pt IDEs and the underlying Ti film, (3) R_{s2} describing the interelectrode resistance of vertically aligned TiO_2 nanotube arrays bridging adjacent Pt IDEs and (4) R_m accounting for the sheet resistance of the unoxidized Ti film at the base of the TiO_2 nanotubes [30]. Compared to the Pt/TiO_2/Ti sensor, the Pt/TiO_2 sensor lacks the unoxidized Ti film at the nanotube base. Consequently, the equivalent circuit diagram for the Pt/TiO_2 sensor was derived from that of the Pt/TiO_2/Ti sensor, as presented in Fig. 6c.

The resistivity of the Ti film is approximately 3.5 Ω·cm [38]. The 4100-fold resistivity difference between the Ti film and TiO_2 (1.44×10^4 Ω·cm) results in the resistance R_{s2} of TiO_2 substantially exceeding the resistance R_m of the Ti film. This disparity causes charge carriers in the Pt/TiO_2/Ti sensor to preferentially migrate through the Ti film when moving between Pt IDEs, following the carrier transfer pathway: Pt → R_{s1} → R_m → R_{s1} → Pt. Conversely, the Pt/TiO_2 sensor exhibits the pathway: Pt → R_{s1} → R_{s2} → R_{s1} → Pt. The Pt/TiO_2/Ti sensor exhibits a higher initial current than the Pt/TiO_2 sensor due to the lower transfer resistance between the Pt interdigital electrodes (IDEs) of the Pt/TiO_2/Ti sensor (Fig. 4a and b). Upon the introduction of hydrogen, hydrogen reacts with adsorbed oxygen on the TiO_2 surface, leading to an increase in the carrier concentration of TiO_2 and a decrease in its resistivity. However, the resistivity remains significantly higher than that of the Ti film. Consequently, the significantly higher carrier transfer resistance in the Pt/TiO_2 sensor accounts for its 10,000-fold lower response relative to the Pt/TiO_2/Ti sensor at room temperature. With increasing operating temperature, accelerated reaction between hydrogen and surface-adsorbed oxygen species on TiO_2 leads to substantial depletion of adsorbed oxygen. This facilitates electron transfer back to the TiO_2 matrix, increasing carrier concentration to a maximum of 2.8×10^{18} cm^{-3} at 150°C under 200 ppm H_2. Consequently, TiO_2 resistivity decreases to 1.75 Ω·cm, rendering R_{s2} and R_m comparable in magnitude. The modulating effect of the Ti film on carrier transport pathways becomes significantly diminished at high temperature. Thus, the response magnitudes of Pt/TiO_2/Ti and Pt/TiO_2 sensors become virtually comparable at elevated temperatures.

Fig. 7a and b displays the response-recovery curves of Pt/TiO_2/Ti and Pt/TiO_2 sensors, respectively, toward 50–2000 ppm hydrogen at room temperature. Response magnitudes extracted from these curves were fitted as shown in Fig. 7c. At 50 ppm hydrogen, both sensors exhibited deviations from the linear fit due to Schottky junction formation at Pt-TiO_2 interfaces. Hydrogen reactions with surface-adsorbed oxygen species facilitate electron transfer back to the TiO_2 matrix, reducing both the depletion width and reverse breakdown voltage of the Schottky junctions [39,40]. When the breakdown voltage falls below the applied sensor bias, current increases substantially. Thus, Schottky junction effects cause response deviations at low concentrations.

Above 100 ppm hydrogen, logarithmic response magnitudes versus logarithmic concentrations follow linear relationships. According to literature [41], this power-law response originates from intergranular Schottky barriers within TiO_2. This indicates that beyond 100 ppm, Pt-TiO_2 interfacial properties remain stable, and sensor responses become predominantly governed by electrical conductivity modulation within TiO_2 nanotubes.

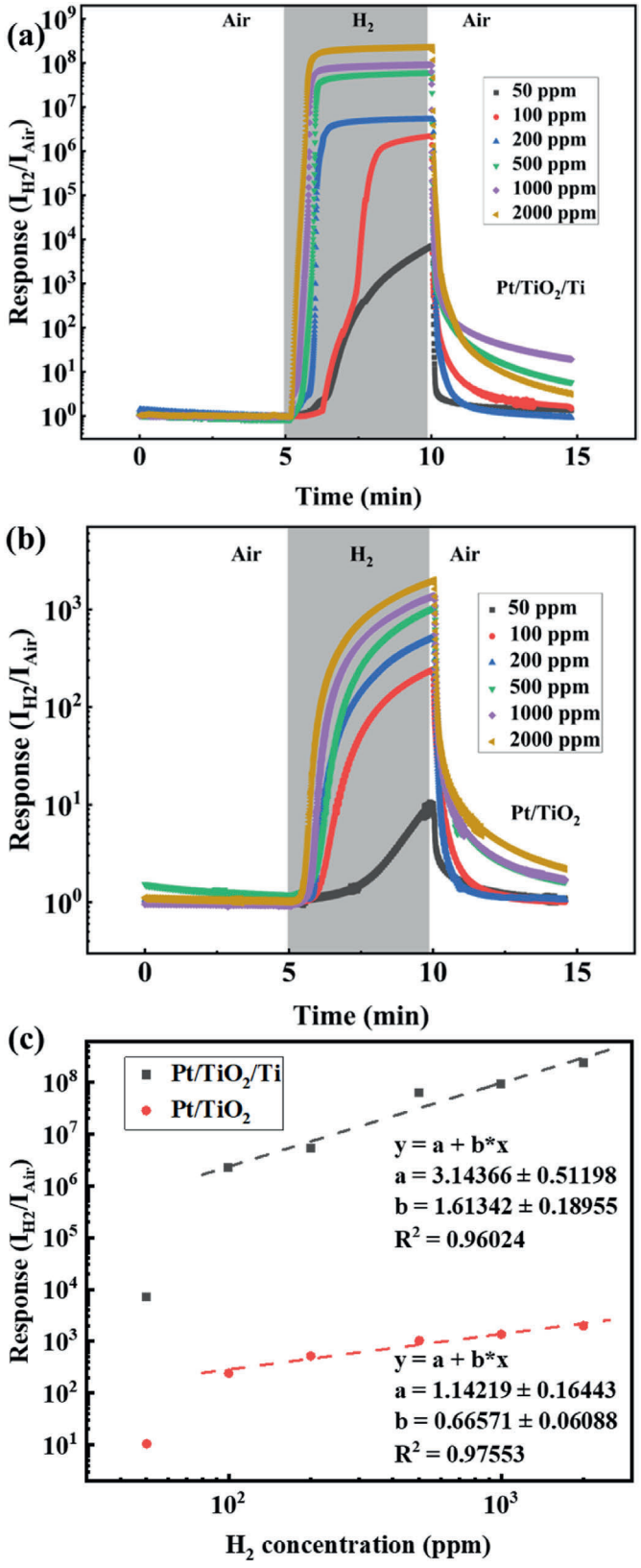

Fig. 7. Response-recovery curves at room temperature toward 50–2000 ppm hydrogen: (a) $Pt/TiO_2/Ti$ sensor, (b) Pt/TiO_2 sensor; (c) Logarithmic plot of hydrogen concentration versus response magnitude.

In Fig. 7c, the linear fit slope of response magnitudes versus hydrogen concentration is 1.61342 for the $Pt/TiO_2/Ti$ sensor, exceeding the 0.66571 slope of the Pt/TiO_2 sensor. This slope disparity is attributed to enhanced electrical conductivity originating from the Ti film at the nanotube base in $Pt/TiO_2/Ti$ devices. As detailed in Ref. [42], such conductivity differences directly amplify slopes.

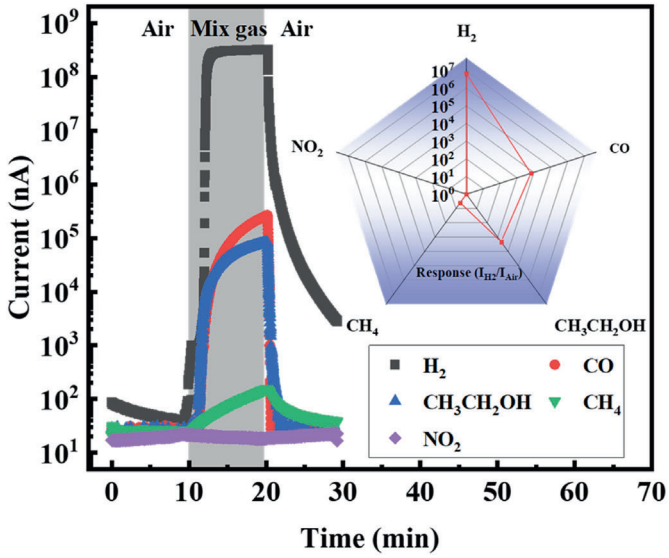

Fig. 8. Cross-sensitivity analysis of the $Pt/TiO_2/Ti$ sensor toward 200 ppm of interfering gases (CO, CH_3CH_2OH, CH_4, NO_2) at 150°C.

Fig. 8 depicts response characteristics of $Pt/TiO_2/Ti$ sensor toward 200 ppm concentrations of H_2, CO, ethanol, CH_4, and NO_2 at 150°C. The four interfering gases were selected based on their relevance to typical gas-sensing environments: three are common reducing agents known to induce cross-sensitivity, and NO_2 represents an oxidizing interferent prevalent in automotive exhaust emissions. The sensor exhibits selectivity toward hydrogen, outperforming its response to other tested gases. For reducing gases, hydrogen possesses superior reducing ability alongside a smaller effective molecular diameter and a higher diffusion coefficient. These properties allow it to more easily enter the interior of the nanotubes and react with the oxygen species adsorbed on the nanotube surface [30,43].

In contrast, as an oxidizing gas, nitrogen dioxide (NO_2) must compete with pre-adsorbed oxygen species to capture electrons from TiO_2. However, the Debye length calculated using the formula from Ref. [32] yields 596.6 nm. This value significantly exceeds half the

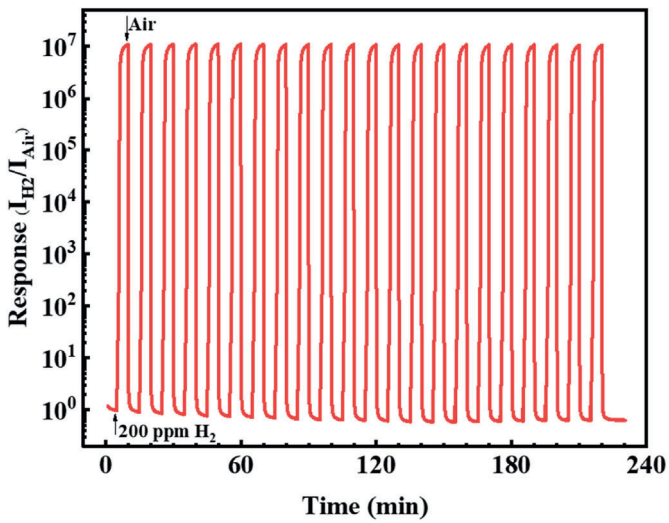

Fig. 9. Repeatability test showing 22 consecutive response cycles at 200 ppm H_2 concentration.

nanotube wall thickness ($t/2 \approx 10$ nm), inducing a flat-band state within the nanotubes [32]. For TiO_2 functioning as an n-type semiconductor, the established flat-band state enhances sensor responses to reducing gases while simultaneously suppressing responses to oxidizing gases.

Fig. 9 illustrates 22 consecutive operational cycles of the sensor exposed to 200 ppm H_2 at room temperature, demonstrating excellent repeatability with 98% response retention over 22 cycles ($\Delta Res./Res._0 = \pm 2.2\%$). The inherent chemical inertness of TiO_2 nanotubes under the measurement atmosphere prevents structural degradation [8]. Meanwhile, the Pt electrode demonstrates excellent catalytic stability in hydrogen and water (the reaction product of hydrogen and surface-adsorbed oxygen), significantly improving the sensor's overall stability. Additionally, the Schottky junction formed at the Pt-TiO_2 interface results in a low and stable baseline current for the sensor in air. These factors enhance the excellent reproducibility of the Pt/TiO_2/Ti sensor.

4. Conclusion

The Pt/TiO_2/Ti sensor exhibited a response of 5.3×10^6 toward 200 ppm hydrogen at room temperature – approximately 10,000 times higher than the Pt/TiO_2 sensor. The performance difference originates from the unoxidized Ti film at the nanotube base in Pt/TiO_2/Ti sensors, which possesses 4100-fold lower resistance than TiO_2. Charge carriers traverse between Pt IDEs preferentially through the conductive Ti film in Pt/TiO_2/Ti devices, whereas conduction in Pt/TiO_2 sensors occurs solely through high-resistance TiO_2 pathways. Consequently, the Pt/TiO_2/Ti sensor demonstrates superior room-temperature gas-sensing performance. Additionally, the Pt/TiO_2/Ti sensor exhibits selectivity and excellent reproducibility.

CRediT authorship contribution statement

Xiaochuan Long: Writing – review & editing, Writing – original draft, Visualization, Validation, Software, Methodology, Investigation, Formal analysis, Data curation, Conceptualization. **Xiao Wen:** Visualization, Investigation, Formal analysis, Data curation, Conceptualization. **Xiao Zhang:** Writing – review & editing, Supervision, Resources, Conceptualization. **Zheng Lu:** Validation, Supervision, Resources, Investigation. **Feng Wei:** Supervision, Resources, Funding acquisition. **Xiaopeng Liu:** Writing – review & editing, Supervision, Resources, Project administration, Funding acquisition, Conceptualization.

Declaration of competing interest

The authors declare that they have no known competing financial interests or personal relationships that could have appeared to influence the work reported in this paper.

Acknowledgement

This work was financially supported by Beijing Nova Program (NO.20230484408), and National Natural Science Foundation of China (NO.52172158).

References

[1] T.T. Tran, V. Bhatt, M.J. Choi, H.T. Nguyen, A. Sharma, M. Kumar, J.H. Yun, Thermal decomposition-assisted, aspect ratio controlled ZnO nanorods towards highly selective H_2 gas detection, Int. J. Hydrogen Energy 84 (2024) 768–779, https://doi.org/10.1016/j.ijhydene.2024.08.252.

[2] G. Pandey, M. Bhardwaj, S. Kumar, S.D. Lawaniya, M. Kumar, P.K. Dwivedi, K. Awasthi, Synergistic effects of Pd-Ag decoration on SnO/SnO_2 nanosheets for enhanced hydrogen sensing, Sensor. Actuator. B Chem. 402 (2024) 135062, https://doi.org/10.1016/j.snb.2023.135062.

[3] T. Hyodo, T. Okusa, W. Sakata, T. Ueda, Y. Shimizu, Impacts of surface modification of Pt-sensing electrodes with Au on hydrogen-sensing properties and mechanism of diode-type gas sensors based on anodized titania, ACS Sens. 8 (2023) 61–70, https://doi.org/10.1021/acssensors.2c01702.

[4] X. Zhang, Y. Xu, H. Liu, W. Zhao, A. Ming, F. Wei, Preparation of porous Co_3O_4 and its response to ethanol with low energy consumption, RSC Adv. 10 (2020) 2191–2197, https://doi.org/10.1039/c9ra08904g.

[5] Y. Tang, Y. Zhao, H. Liu, Room-temperature semiconductor gas sensors: challenges and opportunities, ACS Sens. 7 (2022) 3582–3597, https://doi.org/10.1021/acssensors.2c01142.

[6] X. Wen, X. Liu, J. Meng, Two-dimensional material gas sensor for disease diagnosis, Rev. Mater. Res. 1 (2025) 100106, https://doi.org/10.1016/j.revmat.2025.100106.

[7] C. Meng, Z. Li Lee, Adjustment methods of schottky barrier height in one- and two-dimensional semiconductor devices, Sci. Bull. 69 (2024) 1342–1352, https://doi.org/10.1016/j.scib.2024.03.003.

[8] G. Korotcenkov, Metal oxides for solid-state gas sensors: what determines our choice? Mater. Sci. Eng. B. 139 (2007) 1–23, https://doi.org/10.1016/j.mseb.2007.01.044.

[9] Z. Li, Z. Yao, A.A. Haidry, T. Plecenik, L. Xie, L. Sun, Q. Fatima, Resistive-type hydrogen gas sensor based on TiO_2: a review, Int. J. Hydrogen Energy 43 (2018) 21114–21132, https://doi.org/10.1016/j.ijhydene.2018.09.051.

[10] M. Paulose, O.K. Varghese, G.K. Mor, C.A. Grimes, K.G. Ong, Unprecedented ultra-high hydrogen gas sensitivity in undoped titania nanotubes, Nanotechnology 17 (2006) 398–402, https://doi.org/10.1088/0957-4484/17/2/009.

[11] K. Chen, K. Xie, X. Feng, S. Wang, R. Hu, H. Gu, Y. Li, An excellent room-temperature hydrogen sensor based on titania nanotube-arrays, Int. J. Hydrogen Energy 37 (2012) 13602–13609, https://doi.org/10.1016/j.ijhydene.2012.06.067.

[12] Y. Ling, F. Ren, J. Feng, Reverse bias voltage dependent hydrogen sensing properties on Au–TiO_2 nanotubes schottky barrier diodes, Int. J. Hydrogen Energy 41 (2016) 7691–7698, https://doi.org/10.1016/j.ijhydene.2016.02.007.

[13] E. Isik, L.B. Tasyurek, I. Isik, N. Kilinc, Synthesis and analysis of TiO_2 nanotubes by electrochemical anodization and machine learning method for hydrogen sensors, Microelectron. Eng. 262 (2022) 111834, https://doi.org/10.1016/j.mee.2022.111834.

[14] E. Sennik, Z. Colak, N. Kilinc, Z.Z. Ozturk, Synthesis of highly-ordered TiO_2 nanotubes for a hydrogen sensor, Int. J. Hydrogen Energy 35 (2010) 4420–4427, https://doi.org/10.1016/j.ijhydene.2010.01.100.

[15] S. Rahbarpour, S.M. Hosseini-Golgoo, Diode type Ag-TiO_2 hydrogen sensors, Sensor. Actuator. B Chem. 187 (2013) 262–266, https://doi.org/10.1016/j.snb.2012.11.017.

[16] V. Galstyan, A. Ponzoni, I. Kholmanov, M.M. Natile, E. Comini, S. Nematov, G. Sberveglieri, Reduced graphene oxide–TiO_2 nanotube composite: comprehensive study for gas-sensing applications, ACS Appl. Nano Mater. 1 (2018) 7098–7105, https://doi.org/10.1021/acsanm.8b01924.

[17] G.K. Mor, O.K. Varghese, M. Paulose, K.G. Ong, C.A. Grimes, Fabrication of hydrogen sensors with transparent titanium oxide nanotube-array thin films as sensing elements, Thin Solid Films 496 (2006) 42–48, https://doi.org/10.1016/j.tsf.2005.08.190.

[18] Y. Kimura, S. Kimura, R. Kojima, M. Bitoh, M. Abe, M. Niwano, Micro-scaled hydrogen gas sensors with patterned anodic titanium oxide nanotube film, Sensor. Actuator. B Chem. 177 (2013) 1156–1160, https://doi.org/10.1016/j.snb.2012.12.016.

[19] J. Moon, H.P. Hedman, M. Kemell, A. Tuominen, R. Punkkinen, Hydrogen sensor of Pd-decorated tubular TiO_2 layer prepared by anodization with patterned electrodes on SiO_2/Si substrate, Sensor. Actuator. B Chem. 222 (2016) 190–197, https://doi.org/10.1016/j.snb.2015.08.054.

[20] D.H. Kim, Y.S. Shim, H.G. Moon, H.J. Chang, D. Su, S.Y. Kim, J.S. Kim, B.K. Ju, S. J. Yoon, H.W. Jang, Highly ordered TiO_2 nanotubes on patterned substrates: Synthesis-in-place for ultrasensitive chemiresistors, J. Phys. Chem. C 117 (2013) 17824–17831, https://doi.org/10.1021/jp405150b.

[21] H. Abe, Y. Kimura, T. Ma, D. Tadaki, A. Hirano-Iwata, M. Niwano, Response characteristics of a highly sensitive gas sensor using a titanium oxide nanotube film decorated with platinum nanoparticles, Sensor. Actuator. B Chem. 321 (2020) 128525, https://doi.org/10.1016/j.snb.2020.128525.

[22] R. Kojima, Y. Kimura, M. Bitoh, M. Abe, M. Niwano, Investigation of influence of electrolyte composition on formation of anodic titanium oxide nanotube films, J. Electrochem. Soc. 159 (2012) D629–D636, https://doi.org/10.1149/2.003211jes.

[23] K. Yasuda, J.M. Macak, S. Berger, A. Ghicov, P. Schmuki, Mechanistic aspects of the self-organization process for oxide nanotube formation on valve metals, J. Electrochem. Soc. 154 (2007) C472–C478, https://doi.org/10.1149/1.2749091.

[24] X. Yu, Y. Li, W. Wlodarski, S. Kandasamy, K. Kalantarzadeh, Fabrication of nanostructured TiO_2 by anodization: a comparison between electrolytes and substrates, Sensor. Actuator. B Chem. 130 (2008) 25–31, https://doi.org/10.1016/j.snb.2007.07.076.

[25] S. Berger, J. Kunze, P. Schmuki, D. LeClere, A.T. Valota, P. Skeldon, G. E. Thompson, A lithographic approach to determine volume expansion factors during anodization: using the example of initiation and growth of TiO_2-nanotubes, Electrochim. Acta 54 (2009) 5942–5948, https://doi.org/10.1016/j.electacta.2009.05.064.

[26] J.M. Macak, H. Tsuchiya, L. Taveira, S. Aldabergerova, P. Schmuki, Smooth anodic TiO_2 nanotubes, Angew. Chem. Int. Ed. 44 (2005) 7463–7465, https://doi.org/10.1002/anie.200502781.

[27] S.P. Albu, A. Ghicov, S. Aldabergenova, P. Drechsel, D. LeClere, G.E. Thompson, J. M. Macak, P. Schmuki, Formation of double-walled TiO_2 nanotubes and robust anatase membranes, Adv. Mater. 20 (2008) 4135–4139, https://doi.org/10.1002/adma.200801189.

[28] S. Singh, W.R.T. Barden, P. Kruse, Nanopatterning of transition metal surfaces via electrochemical dimple array formation, ACS Nano 2 (2008) 2453–2464, https://doi.org/10.1021/nn8003789.
[29] A. Thomas, L. Thirumalaisamy, S. Madanagurusamy, K. Sivaperuman, Incompatibility of pure SnO_2 thin films for room-temperature gas sensing application, ACS Omega 8 (36) (2023) 32848–32854, https://doi.org/10.1021/acsomega.3c04038.
[30] M.C.K. Sellers, E.G. Seebauer, Measurement method for carrier concentration in TiO_2 via the Mott-Schottky approach, Thin Solid Films 519 (2011) 2103–2110, https://doi.org/10.1016/j.tsf.2010.10.071.
[31] M. Cerchez, H. Langer, M. El Achhab, T. Heinzel, D. Ostermann, H. Luder, J. Degenhardt, Dynamics of hydrogen sensing with Pt/TiO_2 Schottky diodes, Appl. Phys. Lett. 103 (2013) 033522, https://doi.org/10.1063/1.4816265.
[32] N. Yamazoe, K. Shimanoe, New perspectives of gas sensor technology, Sensor. Actuator. B Chem. 138 (2009) 100–107, https://doi.org/10.1016/j.snb.2009.01.023.
[33] J. Meng, H. Li, L. Zhao, J. Lu, C. Pan, Y. Zhang, Z. Li, Triboelectric nanogenerator enhanced schottky nanowire sensor for highly sensitive ethanol detection, Nano Lett. 20 (2020) 4968–4974, https://doi.org/10.1021/acs.nanolett.0c01063.
[34] L.B. Tasyurek, E. Isik, I. Isik, N. Kilinc, Enhancing the performance of TiO_2 nanotube-based hydrogen sensors through crystal structure and metal electrode, Int. J. Hydrogen Energy 54 (2024) 678–690, https://doi.org/10.1016/j.ijhydene.2023.08.202.
[35] V. Mansfeldova, M. Zlamalova, H. Tarabkova, P. Janda, M. Vorokhta, L. Piliai, L. Kavan, Work function of TiO_2 (anatase, rutile, and brookite) single crystals: effects of the environment, J. Phys. Chem. C 125 (2021) 1902–1912, https://doi.org/10.1021/acs.jpcc.0c10519.
[36] J. Chrzanowski, B. Bieg, Thickness dependence of the work function in case of ultra-thin metallic layers, Appl. Surf. Sci. 540 (2021) 148363, https://doi.org/10.1016/j.apsusc.2020.148363.
[37] Á. Horváth, A. Sulyok, C. Dücső, R. Schiller, Work function of titanium thin layers, J. Appl. Phys. 134 (2023) 144304, https://doi.org/10.1063/5.0169329.
[38] Y.L. Jeyachandran, B. Karunagaran, S.K. Narayandass, D. Mangalaraj, The effect of thickness on the properties of titanium films deposited by dc magnetron sputtering, Mater. Sci. Eng. A. 458 (2007) 361–365, https://doi.org/10.1016/j.msea.2006.12.088.
[39] J. Meng, Z. Li, Schottky-contacted nanowire sensors, Adv. Mater. 32 (2020) e2000130, https://doi.org/10.1002/adma.202000130.
[40] K. Potje-Kamloth, Semiconductor junction gas sensors, Chem. Rev. 108 (2008) 367–399, https://doi.org/10.1021/cr0681086.
[41] Z. Hua, Y. Li, Y. Zeng, Y. Wu, A theoretical investigation of the power-law response of metal oxide semiconductor gas sensors I: schottky barrier control, Sensor. Actuator. B Chem. 255 (2018) 1911–1919, https://doi.org/10.1016/j.snb.2017.08.206.
[42] D.A. Mirabella, P.M. Desimone, M.A. Ponce, C.M. Aldao, L.F. da Silva, A.C. Catto, E. Longo, Effects of donor density on power-law response in tin dioxide gas sensors, Sensor. Actuator. B Chem. 329 (2021) 129253, https://doi.org/10.1016/j.snb.2020.129253.
[43] S. Luo, R. Chen, J. Wang, L. Xiang, Conductometric methane gas sensors based on ZnO/Pd@ZIF-8: effect of dual filtering of ZIF-8 to increase the selectivity, Sensor. Actuator. B Chem. 383 (2023) 133600, https://doi.org/10.1016/j.snb.2023.133600.